



Article

Surface Current Variations and Hydrological Characteristics of the Penghu Channel in the Southeastern Taiwan Strait

Po-Chun Hsu ^{1,2}

¹ Center for Space and Remote Sensing Research, National Central University, Taoyuan 320, Taiwan; hpochun@csrsr.ncu.edu.tw

² Graduate Institute of Hydrological and Oceanic Sciences, National Central University, Taoyuan 320, Taiwan

Abstract: Coastal ocean dynamics application radar (CODAR) SeaSonde high-frequency (HF) radars deployed along the coast of Taiwan were used to reveal ocean surface current variations both hourly and through climatological seasons in the Penghu Channel (PHC), southeastern Taiwan Strait (TS), from December 2014 to December 2020. The ocean current in the PHC has a semidiurnal tidal cycle, and the seasonal main flow, wind direction, and wind strength significantly affect the direction and speed of the flow passing through the PHC. The speed of the tidal current in the PHC area can reach more than 1 m/s, and the monthly average flow speed in the PHC is between 0.12 (winter) and 0.24 m/s (summer). Several buoys indicated that the southward flow along the western coast of Taiwan drifted through the PHC in fall and winter. The HF radar observations confirmed the same, implying that this occurred during the strong northeastern monsoon. For a weak northerly wind or even southerly wind, the flow in the PHC can be northward. Different wind directions can affect the speed of the flow passing through the PHC and the branch flow in the northern PHC. The HF radar results are highly consistent with the spatial characteristics of satellite data regarding the sea surface temperature, sea surface salinity, and chlorophyll concentrations; however, there are significant differences from the satellite-derived ocean current.

Keywords: coastal radar; drifter; ocean currents; sea surface temperature; sea surface salinity; ocean chlorophyll; Kuroshio; Taiwan Strait



Citation: Hsu, P.-C. Surface Current Variations and Hydrological Characteristics of the Penghu Channel in the Southeastern Taiwan Strait. *Remote Sens.* **2022**, *14*, 1816. <https://doi.org/10.3390/rs14081816>

Academic Editor: Silvia Piedracoba

Received: 12 March 2022

Accepted: 6 April 2022

Published: 9 April 2022

Publisher's Note: MDPI stays neutral with regard to jurisdictional claims in published maps and institutional affiliations.



Copyright: © 2022 by the author. Licensee MDPI, Basel, Switzerland. This article is an open access article distributed under the terms and conditions of the Creative Commons Attribution (CC BY) license (<https://creativecommons.org/licenses/by/4.0/>).

1. Introduction

The Penghu Channel (PHC) is located adjacent to southwestern Taiwan (Figure 1) and is a sea area consisting of a narrow and long submarine canyon [1,2]. The PHC is one of the main water routes connecting the South China Sea (SCS), the Taiwan Strait (TS), and the East China Sea (ECS). The PHC has a water depth of approximately 100–200 m, the surface seawater has a semidiurnal tidal cycle [3,4], and the flow in the lower layer experiences turbulent mixing caused mainly by tidal current shear [5]. The ocean currents adjacent to the PHC include the northward Taiwan Strait Current (TSC) from March to September in the TS, the southward China Coastal Current (CCC) in the western TS from October to February, the southward Northern Taiwan Coastal Current (NTCC) in the eastern TS from October to January [6], the Kuroshio Branch Current (KBC) flow from the Pacific into the northern SCS [7], and the SCS Current (SCSC) in the southern PHC [8].

Because the flow path adjacent to the PHC has various water masses and seasonal variations, researchers have not only investigated temperature and salinity [9–12] but have also focused on the composition of chemical elements [13–15] and marine ecology, such as primary productivity and aquaculture [16,17]. The PHC often has typhoons in summer and fall, which disturb the flow field and produce an upwelling of cold water [18]. The PHC is also affected by abnormal cold events in the short term [17,19], and the El Niño Southern Oscillation and Pacific Decadal Oscillation in the long term [13,14]. Some important phenomena that have been studied are summarized as follows: Upwelling can

occur near the PHC and Taiwan Bank in summer, resulting in a high sea surface temperature (SST) gradient, high chlorophyll-a concentration (Chl-a), and significant oceanic front [9]. The Pearl River plume can also intrude into the PHC in summer because of large river discharge and strong southwesterly winds on the shelf [10]. In winter, the mainland coastal cold current can cause cold disasters under strong northeasterly winds and the interaction of current and waves in the northern PHC [19].

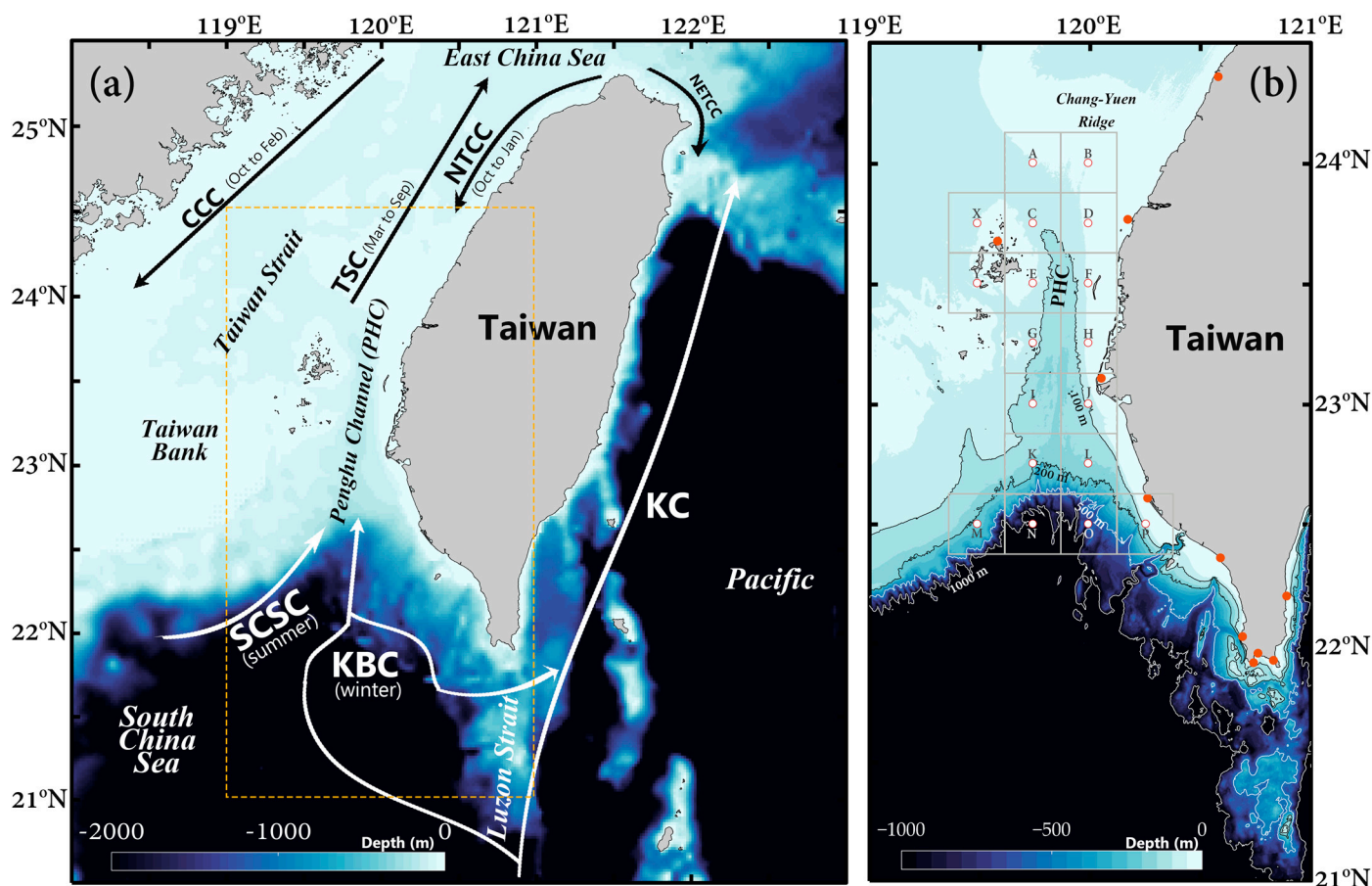


Figure 1. (a) Schematic diagram of the sea area adjacent to Taiwan and its main ocean current. (b) The study area of the Penghu Channel and its submarine topographic characteristics and the observation gridded position from the historical survey. The red dots represent the HF radar stations. Full names of ocean currents: CCC (China Coastal Current), TSC (Taiwan Strait Current), NTCC (Northern Taiwan Coastal Current), NETCC (Northeastern Taiwan Countercurrent), KC (Kuroshio Current), SCSC (South China Sea Current), KBC (Kuroshio Branch Current).

Researchers have given more attention to special, abnormal PHC events and have rarely considered how the general ocean current and its temperature and salinity characteristics are formed. The investigation of flow volume through the PHC has been limited to surveys [20] and numerical models [21]. Researchers have mostly followed results from 20 years ago regarding the current direction and seasonal characteristics in the area adjacent to the PHC [8]. The ocean current flows northward through the PHC from the southwestern Taiwan throughout the year and has different water mass characteristics in different seasons. That is, the KBC in winter and spring and the SCSC in summer and fall. In addition, the currents in the northern PHC all flow northward and enter the middle of the TS or flow along the coast of Taiwan. However, recent studies found that the characteristics of the ocean current flowing northward through the PHC in each season seem to be somewhat inconsistent with new observations, especially in winter. Using drifter data from before 2007, researchers observed that drifters did not flow northward in winter in the northern PHC, and not all trajectories passed northward in the PHC [22]. Recently,

researchers used the geostationary ocean color imager to derive the ocean surface flow and found that the flow field in the northern PHC was, indeed, a southward flow under the strong northeastern monsoon [4]. Other researchers used coastal radar data to confirm that the flow along the coast of Taiwan in the northern PHC is mainly a southward flow in winter, which is called the NTCC [6]. In the western TS, researchers also used coastal radars and drifters to suggest that winds with different intensities could, indeed, significantly change the flow direction in the TS [23,24]. Researchers analyzed the main components of various tides in the TS based on the coastal radar data and empirical orthogonal function method and confirmed that the M2 tidal constituent is dominant, and the maximum speed of tidal currents near the PHC is 1.5 m/s [25]. In addition, researchers speculated that the northeasterly monsoon could cause the ocean current in the TS to flow southward in winter.

It is clear that researchers have different views and have produced new findings on the flow field in the TS. The PHC is an important water route located in the southeastern TS, and it is necessary to clarify the seasonal ocean current characteristics of the PHC before further discussing the whole flow field in the TS in the future. Therefore, the purpose of this study is to use satellite, drifter buoy, and historical survey data to present the ocean current characteristics of the PHC; to use hourly observations of coastal ocean dynamics applications radar (CODAR) SeaSonde HF radars to observe the ocean surface current from December 2014 to December 2020; and to examine whether ocean wind is the decisive factor affecting the PHC flow field. Several issues need to be clarified: (1) Are the direction and speed of ocean currents observed by satellites adjacent to the PHC correct? (2) What is the difference between the ocean surface currents based on satellite and HF radar observations? (3) Does the northward ocean surface current persist in the PHC under strong northeasterly winds? Finally, the spatial distribution of sea surface temperature, salinity, and Chl-a and the seasonal water mass composition in the PHC are discussed.

2. Data

2.1. Ocean Currents

2.1.1. Satellite Observations

The daily instantaneous and monthly mean global ocean gridded level-4 sea surface heights and derived surface geostrophic eastward and northward sea water velocity data on a 0.25° grid from 1993 to the present were provided by the Copernicus Marine Environment Monitoring Service (CMEMS). The reprocessed optimal interpolation data were made by merging all satellite altimeter missions to compute gridded absolute dynamic topography and geostrophic currents.

2.1.2. Survey Observations

The Ocean Data Bank (ODB) database has compiled various oceanographic data from a vessel-mounted acoustic Doppler current profiler (ADCP) manufactured by Teledyne RD Instruments adjacent to the PHC (119–121°E, 21–24.5°N) since 1991, which were collected by R/V Ocean researchers. The measured data underwent quality control labelling by the Global Temperature-Salinity Profile Program (GTSP) of the National Oceanographic Data Center (NODC) and were transformed into a 0.25° grid in latitude and longitude (totals of 18 grid points were used, see Figure 1b), and they were processed into four seasons: winter (December–February), spring (March–May), summer (June–August), and fall (September–November).

2.1.3. SeaSonde HF Radar Observations

The Taiwan Ocean Research Institute, National Applied Research Laboratories, built the Taiwan ocean radar observation system network along the coast of Taiwan [25,26]. SeaSonde, an integrated radar antenna system developed by CODAR Ocean Sensor in the United States, is the high-frequency ocean radar used in this system. The high-frequency ocean radar uses the Bragg resonance of radio waves and the ocean surface to generate backscattering and is based on the Doppler shift between the received echo signal and the

transmitted frequency due to surface currents and then the radial velocity of the ocean surface; that is, the velocity component of the ocean current toward or away from the radar station is calculated. To observe the current velocity vector on the actual ocean surface, at least two adjacent stations must jointly observe the same sea area and then synthesize the generated radial velocity to produce the ocean surface current field (total velocity). In this study, the flow field near the PHC was measured using 11 coastal radar stations (red dots in Figure 1b, including seven, three, and one operational set of 5, 13, and 24 MHz compact-type high-frequency ocean radar instruments, respectively) with an hourly temporal resolution and 10 km spatial resolution from December 2014 to December 2020 [25,27].

2.2. In Situ Observations

2.2.1. Surface Drifter

A total of 37 Global Drifter Program (GDP) hourly drifting buoy locations and velocities from 2000 to 2021 were used. The hourly interpolated dataset was provided by the Atlantic Oceanographic and Meteorological Laboratory Physical Oceanography Division of the National Oceanic and Atmospheric Administration (NOAA). The interpolation methods for drifter trajectories tracked by the Argos system and global positioning system were described previously [28]. Drifter buoys always have drogues at a nominal depth of 15 m underwater. The drogue may be lost in the drifting process; at this time, the drifting path represents the flow direction and velocity of the sea surface and is significantly controlled by the ocean wind and waves. Drifters measure location, and sea surface current velocities (Lagrangian velocities) are calculated from the change in position of the drifter over time.

2.2.2. Historical Hydrological Observations

The seasonal temperature and salinity data adjacent to the PHC on a 0.25° grid from 1985 to the present were observed by a conductivity temperature depth profiler and obtained from the ODB of the Ministry of Science and Technology, Taiwan. Totals of 18 grid points were used (Figure 1b). The temperature sensor measured the seawater temperature, and the conductivity sensor measured the conductivity and converted it into a further-calculated salinity value. Data quality control was performed by the NODC's GTSP.

2.3. Temperature, Salinity, Chlorophyll Concentration, and Wind

The monthly mean Himawari-8 level-3 SST data with a 2 km spatial resolution [29,30] and level-3 Chl-a data with a 5 km spatial resolution [31] from August 2015 to the present were supplied by the P-Tree System, Japan Aerospace Exploration Agency. The monthly mean multi-observation global ocean sea surface salinity (SSS) level-4 data on a 0.25° grid from 1993 to the present were provided by the CMEMS. The dataset was obtained through an optimal interpolation algorithm that combines the soil moisture and ocean salinity satellite readings and in situ salinity measurements [32]. The global ocean wind level-4 reprocessed monthly mean observation data on a 0.25° grid from May 2007 to December 2020 were provided by the CMEMS. The dataset was estimated from daily global wind fields calculated and derived from ASCAT scatterometers onboard the METOP-A and METOP-B satellites. The three-day average ASCAT-A ocean wind data were produced by remote sensing systems and sponsored by the National Aeronautics and Space Administration (NASA).

3. Ocean Currents Adjacent to the PHC

Satellite ocean current data are easy to obtain and have high spatial coverage, but the daily instantaneous data are interpolated grid data and only represent the geostrophic flow field. Cruise observation can obtain the ocean current characteristics of the whole layer of water at a specific location, but this measurement only represents the results of a specific time. Even if these data are further averaged into seasonality, they still only represent the results in good sea conditions in each season. The flow trajectory obtained by the deployed

drifter can represent the possible path of ocean current and material transportation in the ocean, but only a few data can be used for case analysis. Therefore, the HF radars are the most suitable tool for nearshore ocean current observation because they provide a high spatial resolution and hourly continuous data. In this section, various ocean current databases are used to present and explain the flow field characteristics adjacent to the PHC and compare the differences between satellite and HF radar data.

3.1. Satellite Observation and Historical Survey Measurements

Satellite observations are usually required to obtain the complete spatial distribution characteristics of the flow field due to existence of ocean currents from various directions and sources in southwestern Taiwan. Figure 2 presents the seasonal flow field adjacent to the PHC observed from the satellite. The four seasons are defined as spring (March–May), summer (June–August), fall (September–November), and winter (December–February). In fall, winter, and spring, the KBC flows into the Luzon Strait to the southern TS, most often from October to March [7]. The flow is characterized by a counterclockwise elliptical loop current (Figure 1) with a range of influence of 250 km². In spring and fall, one branch of the KBC in the western loop current can move northward into the PHC. In summer, the SCS surface current flows into the PHC. The satellite observed that the speed of the northward flow adjacent to the PHC has clear seasonal variations, as the speed of the northward flow in spring (0.34 m/s) and summer (0.45 m/s) is faster than in fall (0.22 m/s) and winter (0.18 m/s). According to a recent study in the northern TS and southern ECS [6], the satellite-derived flow field was clearly different from the real condition of ocean surface currents, especially in winter. The main reason for this is that the interval of satellite orbit revisits is too long, and the spatial resolution is not sufficiently high. Are the direction and speed of ocean currents observed by satellites adjacent to the PHC correct? The long-term survey observation data of 10 stations in the PHC (Figure 3) were used to compare with satellite-derived ocean current. The ocean current speeds of the upper 20 m in each season were 0.28 m/s (winter), 0.37 m/s (spring), 0.54 m/s (summer), and 0.25 m/s (fall), which were slightly faster than the average speed of the satellite-derived data. In addition, the first layer (10 m) of survey observations presented that the flow direction of meridional components was different from the satellite observations. In winter, meridional components of -0.64 m/s and -0.29 m/s were observed in the western PHC (Stations X and Y). In fall, southward flow was also observed at several locations, especially in the middle of the PHC where the meridional components of -0.61 m/s (Station X), -0.42 m/s (Station E), -0.19 m/s (Station Y), and -0.14 m/s (Station F) were observed. In addition, the survey observation also presented that the meridional components of the long-term average current were close to zero, which suggests that there is a certain proportion of southward flow in the PHC. From the results of the whole layer of water, the flow speed and direction near the surface (10 m) were inconsistent with the deeper flow, and the surface flow might have been significantly affected by the wind. The average wind direction and speed in the PHC (119.5–120.5° E, 23–24° N) in the four seasons were: northeasterly, 11.4 m/s (winter); northeasterly, 7.4 m/s (spring); southerly, 9.8 m/s (summer); and northeasterly, 8.3 m/s (fall). Does the northward ocean surface current persist under strong northeasterly winds? Since the survey observation was like random data of observation samples with good sea conditions, whether the southward flow was an accidental event or a long-term characteristic could not be determined here. The trajectory analysis of the drifter buoy may help to clarify this.

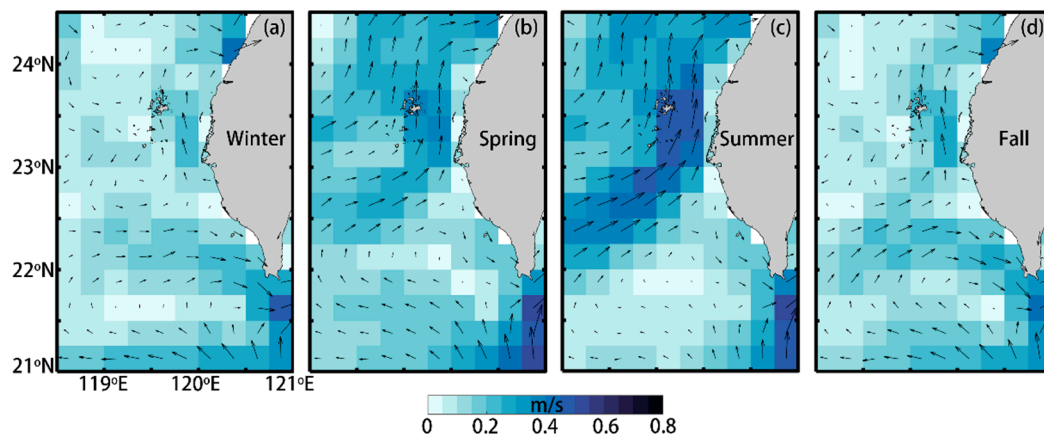


Figure 2. Climatological seasonal satellite-derived geostrophic ocean currents averaged over time from 1993 to 2020: (a) winter, (b) spring, (c) summer, and (d) fall. The variance of ocean current speed is presented in Figure A1 in Appendix A.

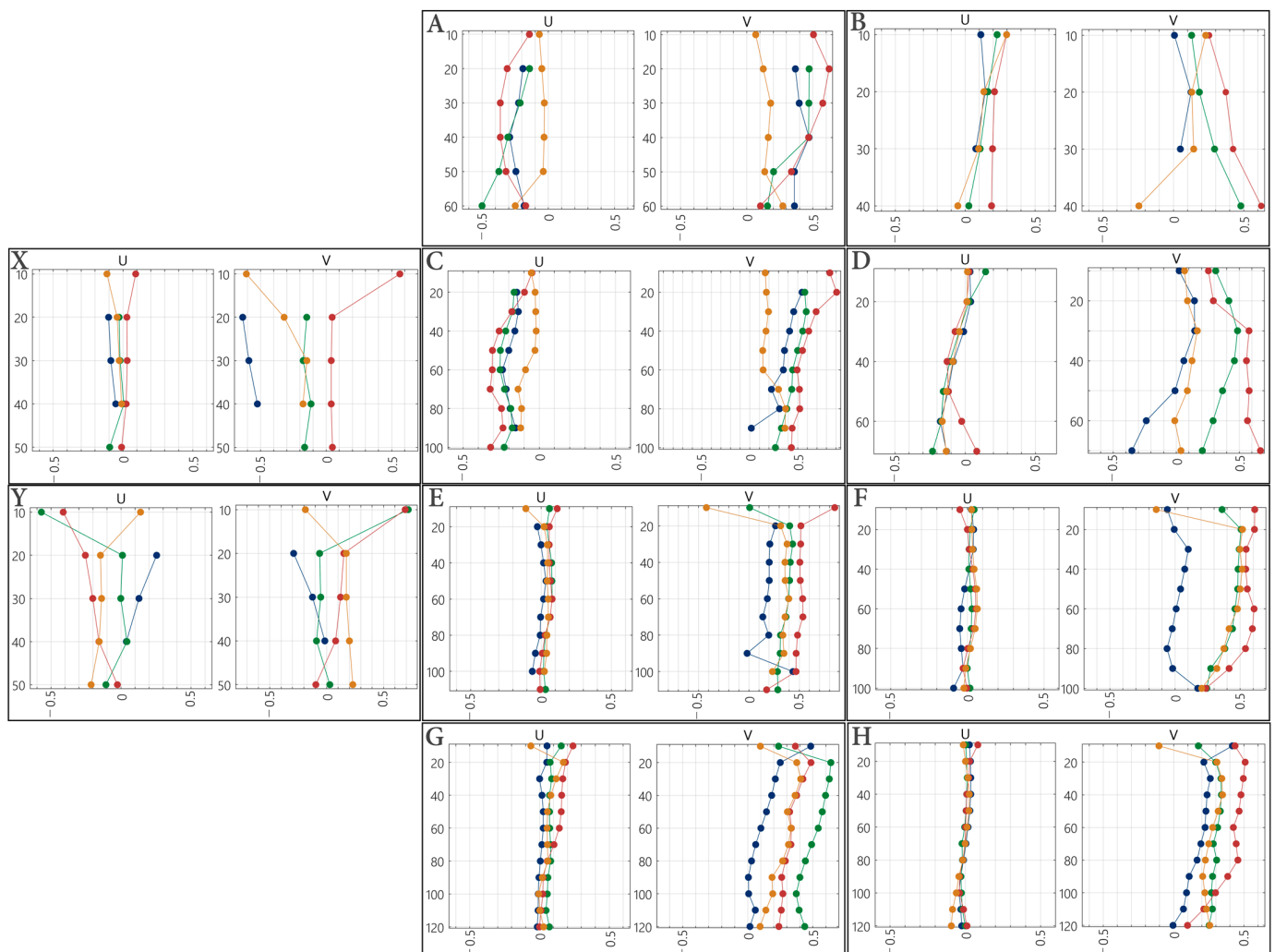


Figure 3. Survey observation of the ocean currents at 10 stations (A–H,X,Y) in the PHC (Figure 1b): winter (blue), spring (green), summer (red), and fall (yellow). The horizontal and vertical coordinates represent the speed (m/s) and water depth (m), respectively. U and V represent the zonal and meridional components of flow, respectively.

3.2. Drifter Trajectories

A total of 37 trajectories of drifters were observed to flow into the PHC, and these were classified according to seasonality (Figure 4). All trajectories in spring (0.10–0.88 m/s) and summer (0.19–1.21 m/s) showed that they flowed in a northern direction across the PHC. In fall, there were four trajectories northward passing through the PHC, with speeds ranging from 0.44 to 0.67 m/s, and two trajectories southward reaching the PHC and hitting the Penghu Islands, with speeds of 0.26 m/s and 0.64 m/s, respectively. The situation in winter was more complicated: one drifter passed northward through the PHC (0.41 m/s), three drifters passed southward (0.10, 0.40, and 0.52 m/s), and the other two drifters started flowing northward (0.10 and 0.52 m/s) but suddenly turned southward in the PHC (0.30 and 0.57 m/s).

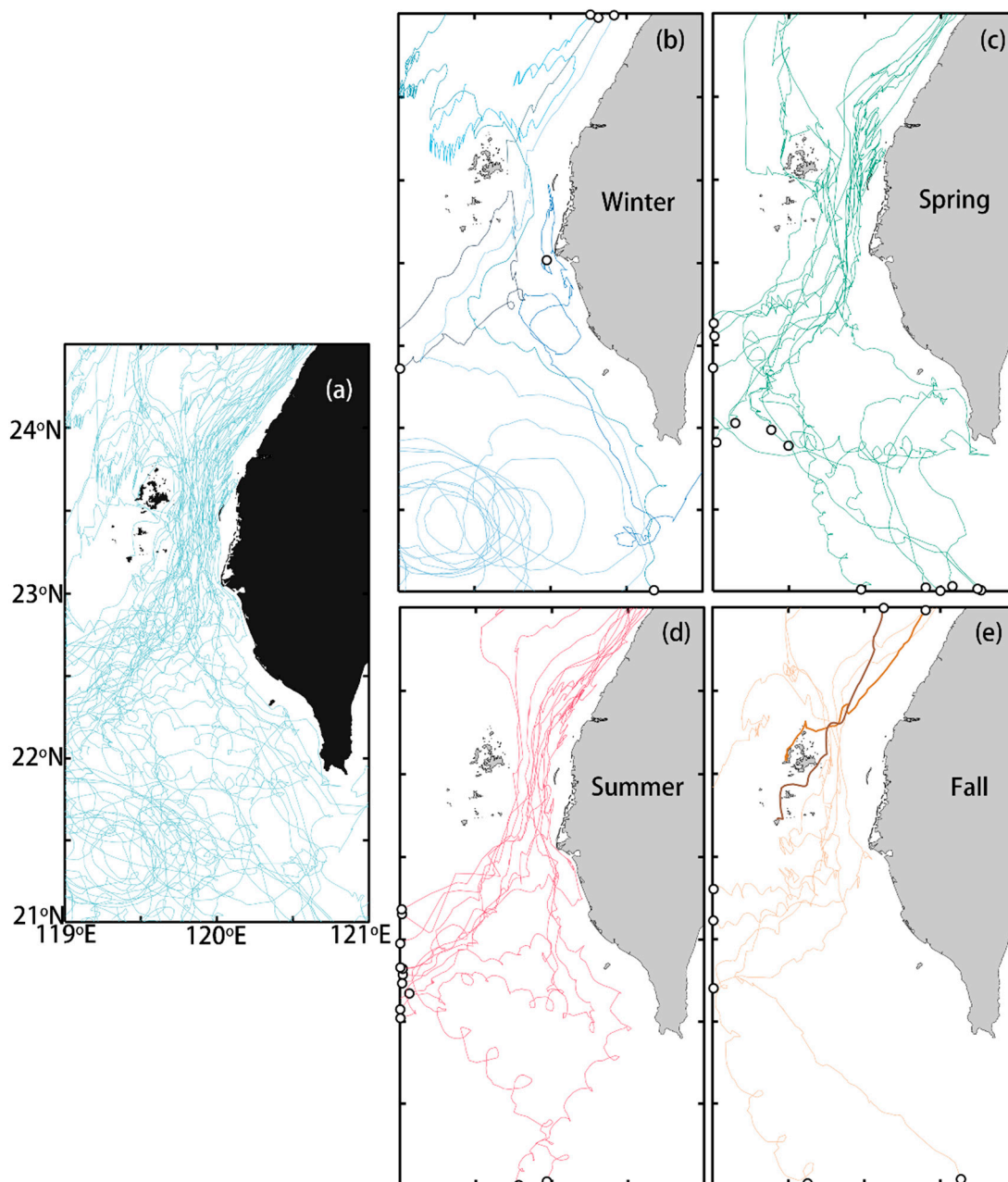


Figure 4. Drifters flowed into the PHC in (a) all periods ($n = 37$), (b) winter ($n = 6$), (c) spring ($n = 13$), (d) summer ($n = 12$), and (e) fall ($n = 6$). The white dots represent the starting position of the drifter deployed or flowing into the study area.

The ASCAT-A ocean wind data are helpful for understanding this phenomenon. The only case in fall after 2007 was the southward flow under the northeasterly wind (16.3 m/s, twice the average in fall), which could be the reason why this drifter flowed southward. In winter, the three cases of drifters drifting southward were all under the strong northeasterly wind (13.2, 13.6, and 17.8 m/s); the northward drifter was under the weak northeasterly wind (8.3 m/s); and the drifter that suddenly turned was first affected by the weak northeasterly wind (6.4 m/s) and then the wind became stronger to 9.5 m/s, which could be the reason for the sudden turn southward. It is worth noting that these hourly drifter trajectories were interpolated from six-hourly data, and there were some differences under significant semidiurnal tidal currents in the TS [4]. Most hourly trajectories did not have significant tidal cycles. However, these real cases suggest that the strong northeasterly monsoon could be the key factor causing the southward flow in the PHC in fall and winter; therefore, it is still valuable to judge the flow direction adjacent to the PHC.

3.3. HF Radar Observations

According to the above three observation results, in the PHC, there were various variations in flow in fall and winter. Therefore, the hourly HF radar data, as the fourth kind of observation, were used, which are some of the most complete space coverages and close to the real conditions. Figure 5 presents the climatological seasonal flow field from the HF radar. A significant KBC was observed in southwestern Taiwan in fall, winter, and spring, with the position of the northern boundary at approximately 22.5°N. The source of the flow in the PHC in spring was obviously from the KBC, while the source in summer was the SCSC. There were two branches after the surface current passed through the PHC in spring: the branch on the west was along the Change-Yuan ridge (Figure 1b), and the branch on the east was along the western coast of Taiwan. In summer, a fast northward current flowed along the coast of Taiwan. In fall, a weak northward flow existed in the PHC, while there existed a U-shaped southwest-northwest flow field in the northern PHC, which was similar to the drifter trajectory (Figure 4e). In winter, there was an obvious southward flow near the coast in the northern PHC, which belonged to the southern end of the NTCC (Figure 1a). There was no obvious meridional flow in the PHC, but there existed a westward flow field, and there was a significant southward flow outside the PHC.

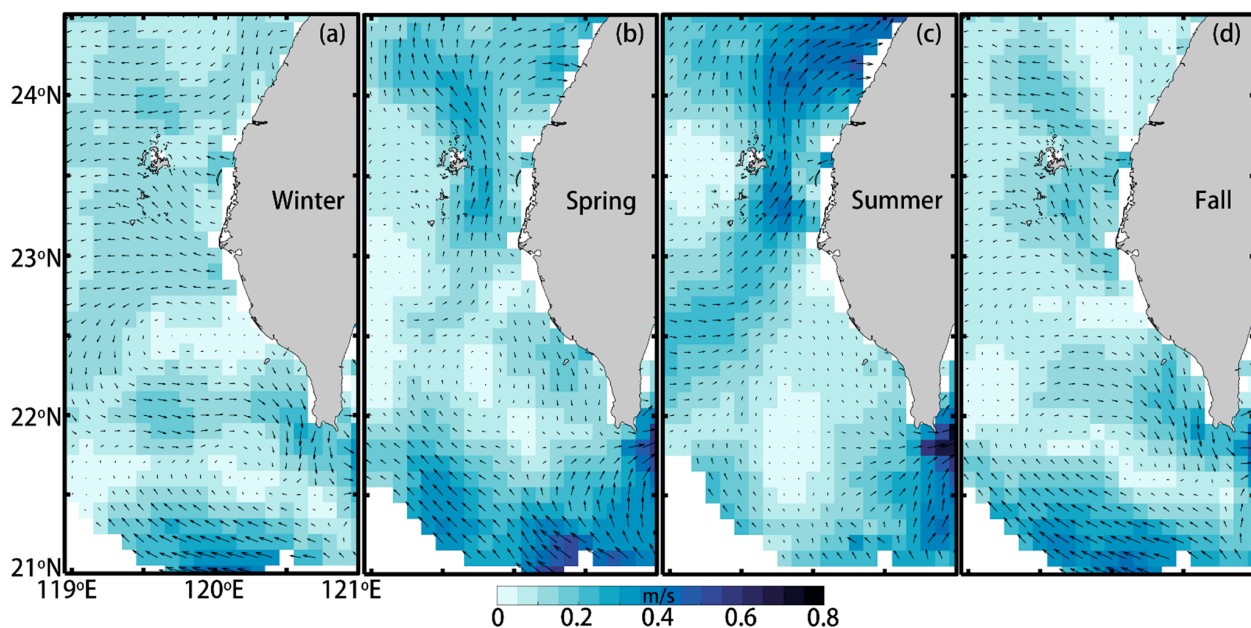


Figure 5. Climatological seasonal flow field averaged from hourly HF radar data from December 2014 to December 2020: (a) winter, (b) spring, (c) summer, and (d) fall. The variance of ocean current speed is presented in Figure A2 in Appendix A.

Do the flow fields in the northern and southern parts of the PHC differ on a monthly timescale? Taking the Penghu Islands as the boundary, the PHC was divided into a northern part (23.7–24°N, 119.7–120°E) and a southern part (23–23.6°N, 119.7–120°E) to compare the differences of flow field in each season (Figure 6). During the December 2014 to December 2020 period, the flow field was stable in spring and summer, and northward flow occurred in each month (Figure 6b,c), with speeds of 0.20 m/s and 0.25 m/s, respectively. In fall, there were five months of ocean surface currents that flowed southward in the northern PHC and northward in the other 13 months. Under both conditions, the average speed was 0.14 m/s; northward flow occurred in the southern PHC in each month with an average speed of 0.16 m/s. This indicates that the southward flow of the drifter buoy was not a frequent event in fall, only occurring under strong northeasterly wind (Figure 4e). In winter, 12 months of surface currents flowed southward in the northern PHC with an average speed of 0.15 m/s, and the speed was only 0.1 m/s in the other seven months. In the southern PHC, there were only two months in which the surface currents flowed southward, and the average speed was 0.12 m/s.

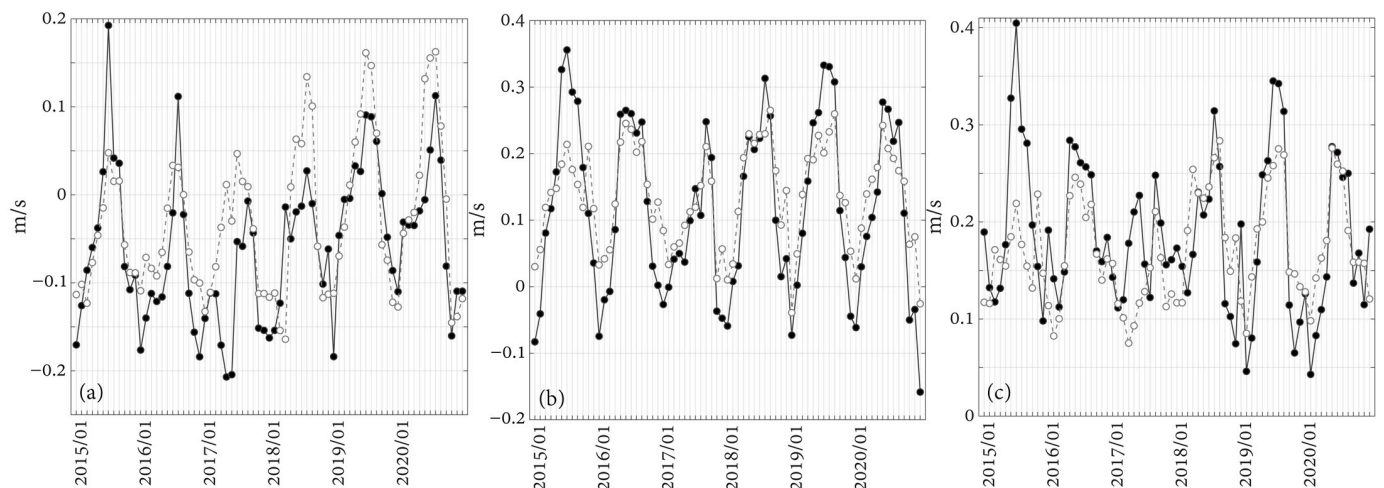


Figure 6. The time series of ocean current velocity in the northern PHC (solid line with black circle) and southern PHC (dashed line with white circle) in each month. (a) Zonal component, (b) meridional component, and (c) flow speed.

Combining the drifter trajectory with the flow field of HF radar more clearly explains why such a path occurred (Figure 4). Figure 7 presents six drifter cases and the average flow field when the drifter passed through the PHC. Figure 7a–c shows the drifting path in the case of high northeasterly wind speed in November and December. The trajectories of these drifters were completely consistent with the HF radar flow field. Figure 7a shows that the drifter quickly passed through the PHC and then flowed to the SCS along the western side of the eddy under a northeasterly wind of 13.6 m/s. Figure 7b,c also shows that, under northeasterly winds of 17.8 m/s and 16.3 m/s, the drifter quickly flowed southward to the PHC and then hit the Penghu Islands and stopped. The above three drifters all flowed southward from the southern ECS (northern Taiwan), which is part of the NTCC (Figure 1a). Figure 7d shows an example in summer under the southwesterly wind (5.8 m/s). The drifter flowed into the PHC along the SCSC from the northern SCS and continued along the western coast of Taiwan to the southern ECS. The two drifters in spring that were close in time were both under northeasterly winds of 8.1 and 8.7 m/s (Figure 7e,f).

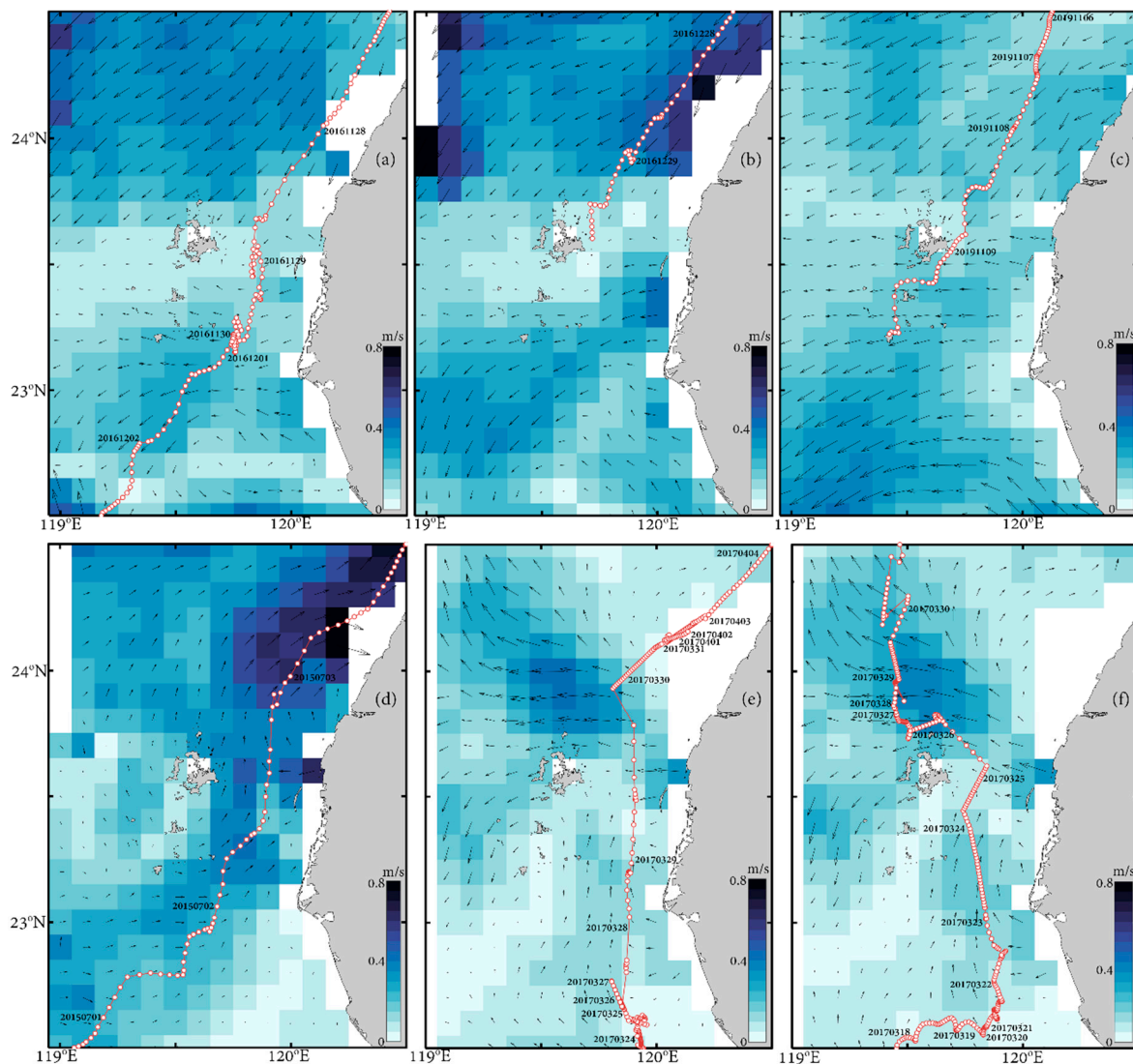


Figure 7. Cases of the drifter trajectory (white dots with red lines) and ocean flow field during buoy drift adjacent to the PHC. The shading color is the average speed of ocean currents observed by HF radar. Drifter ID: (a) 127384, (b) 127386, (c) 66410930, (d) 127423, (e) 63942870, and (f) 63942890.

To determine whether wind direction and wind speed are important factors determining the PHC flow field, the ASCAT-A ocean wind data and HF radar data were combined to classify ocean wind conditions in each season (Figure 8). The calculation area of ocean wind was only focused on the PHC. In winter, the PHC was under a northerly wind almost every day. According to the wind speed, it was divided into weak (<10 m/s), moderate (10–14 m/s), and strong (>14 m/s). The results suggest that the southward NTCC continued to pass through the PHC and enter the SCS under a strong northerly wind (Figure 8c), and the northward flow passed through the PHC and flowed westward into the middle of the TS under a weak northerly wind (Figure 8a). The flow field in the moderate northerly wind was similar to the long-term average flow field in winter (Figure 8b). The flow in the PHC was stable northward in spring and summer, but the direction of the wind direction changed slightly in these two seasons. As mentioned above, there could be two branches after the northward flow passed through the PHC in spring (Figure 5b). The results suggest that the flow speed of the branch toward the coast of Taiwan was faster under the southerly wind (Figure 8d); the flow speed of the branch toward the middle of the TS was faster under the northerly wind (Figure 8e). In summer, the northward flow passing through the PHC with the southerly wind (Figure 8f) was significantly faster than that with the

northerly wind (Figure 8g). In fall, there were several days in the case of the southerly wind when the flow passed northward through the PHC (Figure 8h), while, in the case of the northerly wind, the impact of the flow under different northerly wind speeds (Figure 8i–k) was similar to the patterns in winter. The results suggest that wind direction and wind speed have a decisive impact on the characteristics of ocean surface currents in the PHC.

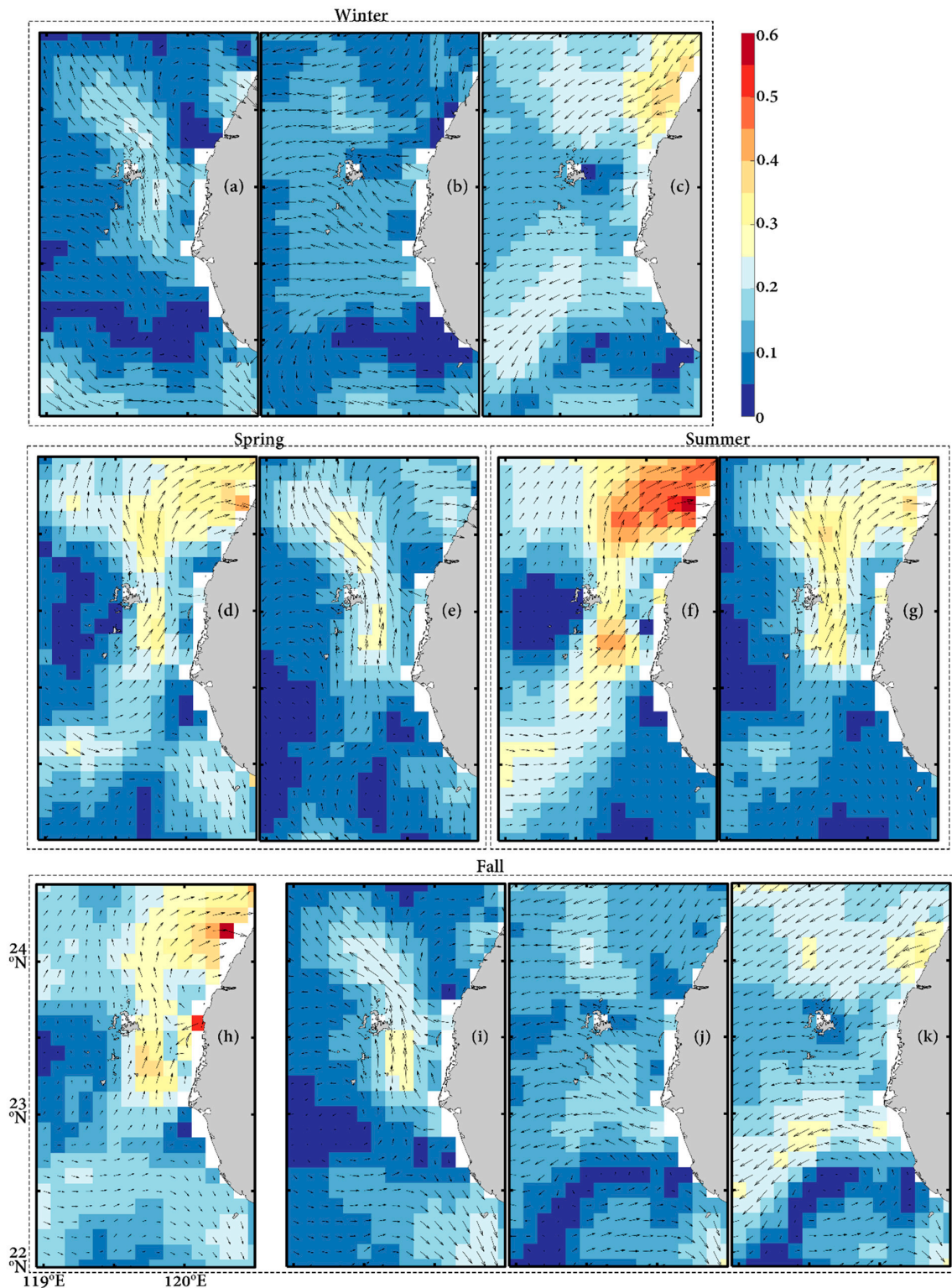


Figure 8. Characteristics of the ocean surface flow field (m/s) adjacent to the PHC under different seasons and ocean wind conditions. Winter: (a) wind speed < 10 m/s ($n = 148$), (b) $10 \leq$ wind speed

≤ 14 m/s ($n = 278$), and (c) wind speed > 14 m/s ($n = 146$); spring: (d) southerly wind ($n = 135$) and (e) northerly wind ($n = 416$); summer: (f) southerly wind ($n = 398$) and (g) northerly wind ($n = 147$); and fall: (h) southerly wind ($n = 52$), (i) northerly wind speed < 10 m/s ($n = 227$), (j) $10 \leq$ northerly wind speed ≤ 14 m/s ($n = 185$), and (k) northerly wind speed > 14 m/s ($n = 82$). n is the number of days.

3.4. Comparison of Ocean Surface Currents between the Satellite-Derived and HF Radar Data

The seasonal variation in the flow field in the PHC and its generation mechanism were clearly clarified in the previous section. Another interesting question is, what was the difference between the ocean surface currents based on satellite and HF radar observations? An example of the flow field in summer (July 2019) and in winter (December 2020) was selected and is presented in Figure 9. The PHC area is an ocean basin with semidiurnal tidal characteristics in the meridional direction. Therefore, there was no significant periodic variation in the zonal component (Figure 9a,c), but obvious tidal signals were observed in the meridional component with ebb and flood tides twice a day (Figure 9b,d). The tidal current speed in an hour could reach 1 m/s. The dotted box in Figure 9a–d presents the spring tide period, but it was found that the flow speed during the spring tide period was not significantly faster in the long-term observation. The reason for this could be that the variation in the main flow caused by wind was more significant than that of the tidal current. Most daily meridional components in July 2019 were northward currents due to the influence of the main flow in the southerly wind (Figure 9f). The wind direction turned northerly from 16 July to 20 July and from 29 July to 30 July; therefore, the speed of the meridional components was much lower than that on other days (Figure 9f). In contrast, there was a northerly wind every day in December 2020, and the meridional component of speed was -0.13 m/s at high wind speeds (16 days) and -0.01 m/s at medium wind speeds (15 days). The comparison between the flow speed and its components based on satellite and HF radar observation is shown in Figure 9e–j, which clearly shows that the value of satellite-derived flow speed was too smooth, and there was an obvious difference between these two datasets on a daily timescale, not to mention that the hourly tidal current signal could not be obtained from the satellite dataset.

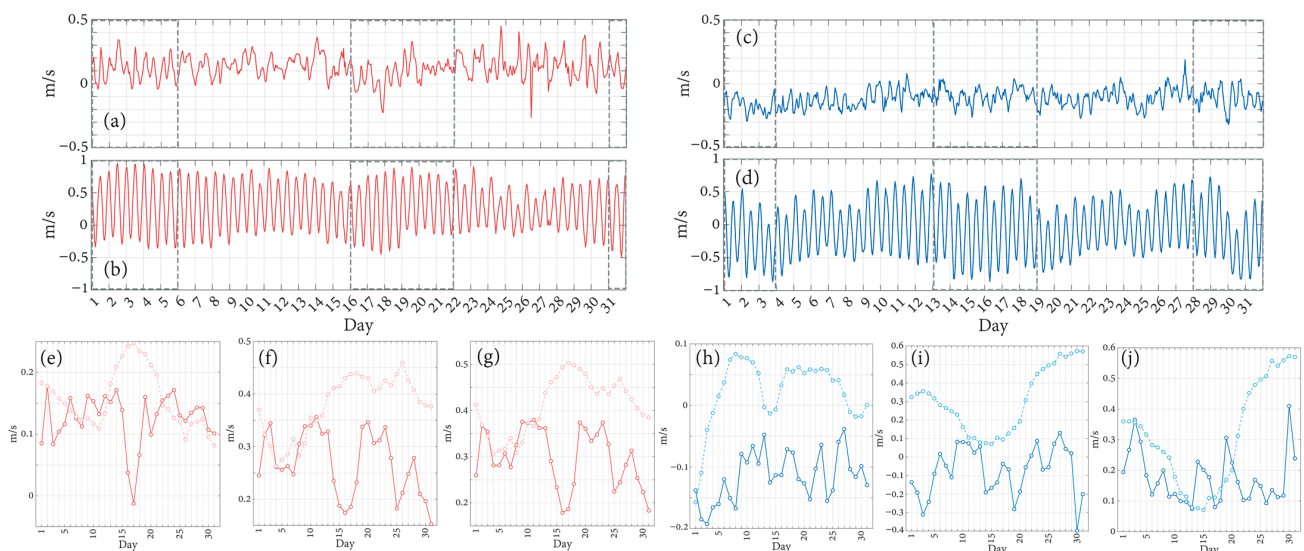


Figure 9. The time series of (a,c) zonal and (b,d) meridional components of ocean surface currents in the PHC observed by HF radar in July 2019 (red line) and December 2020 (blue line), respectively. The dashed box represents the time of spring tide. The time series of the daily average (e,h) zonal component, (f,i) meridional component, and (g,j) flow speed from satellite (dashed line) and HF radar observations (solid line) in July 2019 (red line) and December 2020 (blue line), respectively.

Does the satellite flow field data in the PHC have any reference value? Figure 10 shows the time series of flow speed observed by satellite and HF radar on a monthly timescale. Obviously, the speed value in the component from satellite data was faster than that observed by HF radar, and the direction of flow was slightly inconsistent, but it still maintained periodic seasonal variation. Comparing the velocity components and their values from each season, the results suggest that there was a high correlation in spring and fall under the monthly timescale between the two datasets. The correlation coefficients of the zonal component, meridional component, and flow speed were 0.68, 0.60, and 0.55, respectively, in spring; in fall, they were 0.65, 0.83, and 0.53, respectively. Although the correlation coefficient of the zonal component was as high as 0.76 in summer, the correlation coefficients of the meridional component and flow speed were only 0.16 and 0.29, respectively. The difference in the value of flow speed between the two datasets was largest in winter, with a low correlation coefficient. The average speed in the PHC observed by HF radar was 0.12 m/s (winter), 0.19 (spring), 0.24 (summer), and 0.14 m/s (fall).

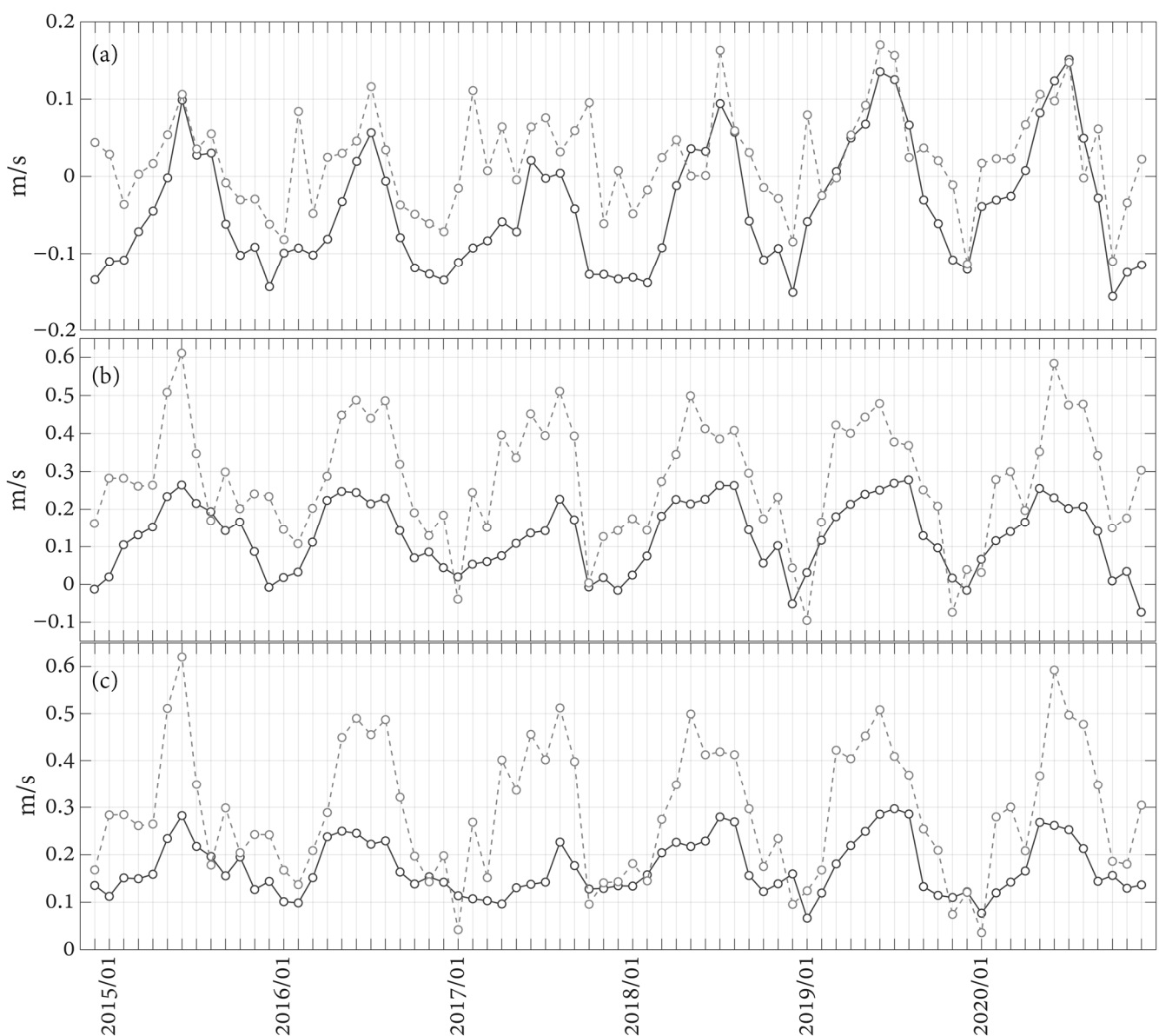


Figure 10. The time series of the monthly average (a) zonal component, (b) meridional component, and (c) flow speed from satellite (dashed line) and HF radar observations (solid line) in the PHC from December 2014 to December 2020.

In summary, the hourly semidiurnal tidal current variation was not observed in the PHC from satellite data and was significantly different from HF radar data on a daily scale (Figure A3 in Appendix A). On a monthly scale, the trend of ocean surface currents observed from satellites in spring and fall may have been close to the real conditions, but it should be noted that the value of speed may have been slightly faster. In winter, satellite data should be used carefully.

4. Hydrological Characteristics Adjacent to the PHC

The spatial characteristics of climatological seasonal SST (Figure 11), Chl-a concentration (Figure 12), and SSS (Figure 13) in the PHC are presented in this section. Based on the knowledge of ocean current characteristics in the previous section, it can now be understood why such hydrological feature distributions appear and what other detailed information is worth examining in the future. The SST and Chl-a concentrations observed by the geostationary Himawari-8 satellite can be used to better observe the changes in the sea surface and reduce the lack of data caused by clouds.

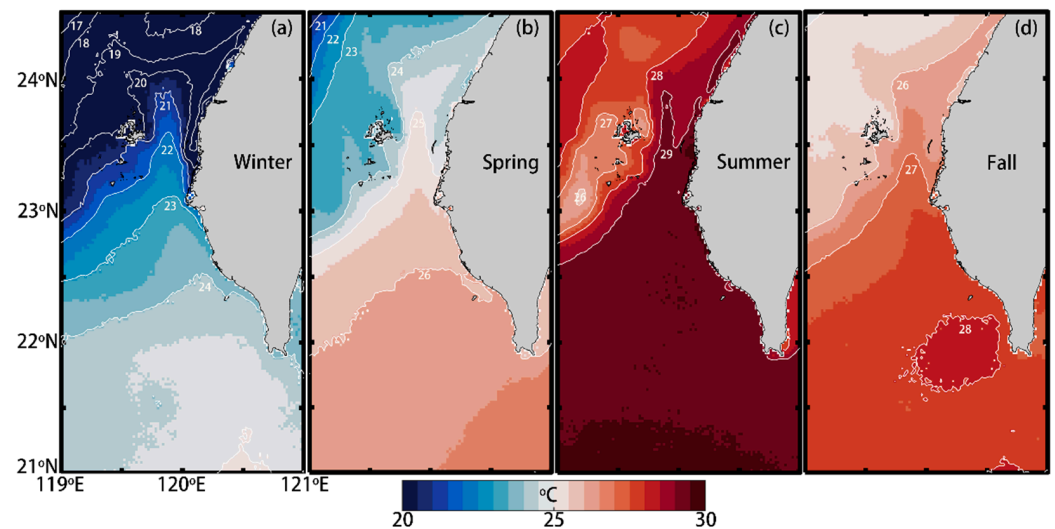


Figure 11. Climatological seasonal SST characteristics adjacent to the PHC from August 2015 to February 2021: (a) winter, (b) spring, (c) summer, and (d) fall.

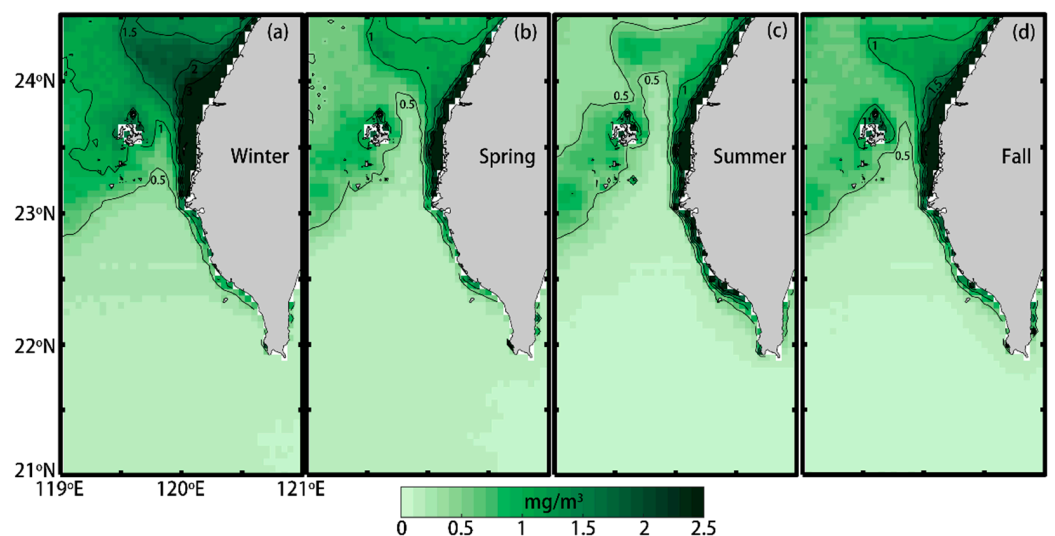


Figure 12. Climatological seasonal chlorophyll-a concentration characteristics adjacent to the PHC from August 2015 to February 2021: (a) winter, (b) spring, (c) summer, and (d) fall.

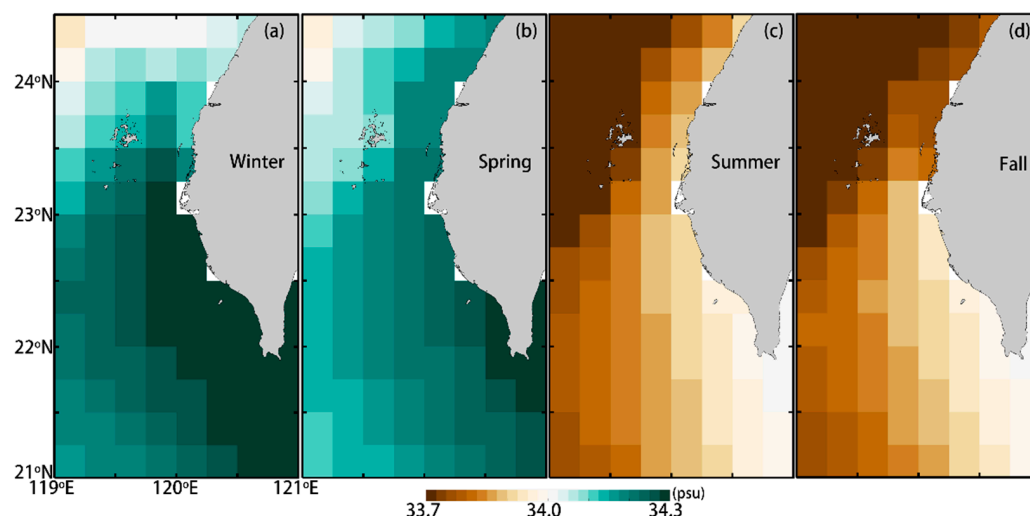


Figure 13. Climatological seasonal SSS characteristics adjacent to the PHC from January 1993 to December 2020: (a) winter, (b) spring, (c) summer, and (d) fall.

In winter, the results show that the northward, warm KBC and southward, cold NTCC met in the northern PHC (Figure 11a), and there was an isotherm deflecting westward, which was consistent with the flow field (Figure 5a). There was an arc isotherm in the northern PHC where the NTCC flowed southward. The Chl-a concentration contour of 1 mg/m^3 (Figure 12a) and the distribution of high SSS (Figure 13a) were also evidence of KBC intrusion. An interesting feature is that a high Chl-a concentration area along the coast of Taiwan was pushed westward and extended into a triangle shape in each season. This may have been a plume generated by the Choushui River, which is the second largest watershed area and the third largest streamflow in Taiwan. Future research should focus on these issues.

The characteristics of SST and Chl-a concentrations were similar in spring, summer, and fall, but some details are still worth noting. In spring, the features of two branches flowing in the northern PHC appeared in the SST field (Figure 11b), and the westward flow (24°C isotherm) was significantly higher than the eastward flow (23.5°C isotherm) because the proportion of westward flow was three times that of the eastward flow (Figure 8d,e). In summer, there was an obvious, cold-water area in the western PHC, which is called the Taiwan Bank, the famous upwelling area of Taiwan (Figures 11c and 12c), and there was often a low SST and high Chl-a concentration. The seasonal average SSS was significantly different, and the main sources of ocean surface currents caused the characteristics of the PHC in winter and spring (high salt, 34.2 psu) and summer and fall (low salt, 33.8 psu).

With a new understanding of the seasonal flow field of the PHC, it is also necessary to compare the water masses observed by surveys with satellite data in each season. Analyzing the characteristics of water masses not only provides an understanding of the source of ocean currents but also furthers knowledge of the characteristics of temperature and salinity underwater [33,34]. Since previous studies did not perform hydrological analyses for the PHC area, this study combined the results of previous studies adjacent to the TS as a reference for the definition of water mass [33–36]. The definition of each water mass is listed in Table 1. A total of 16 spatial grid datapoints from historical surveys adjacent to the PHC were selected to examine seasonal variations (Figure 14). The types of water mass in spring and summer were clear. The water masses in spring were the KBW, KSSW, and KIW (Figure 14c) from the upper layer to the lower-layer depth. The temperature and salinity curves of each station were similar, and the values of surface water from the survey were also quite consistent with satellite observations, which indicates that the main flow source in the PHC was single and stable in spring. The water masses in summer were the SCSSW, SCSW, KSSW, and KIW from the top to bottom of the water layer (Figure 14d). In addition to the fresher upper water observed by the survey at Stations G and P, the salinity

results at each station were also much lower than those observed by satellite. Because the survey covered only a few specific times, it is difficult to determine whether the dilution of the water was due to the rainfall brought by the typhoon in summer [37] or river runoff was not captured by satellite. Further use of onsite observations is needed in the future. The upper-layer water mass in fall was composed of the SCSW, KBW, and MCCW. It is worth noting that low-salt water (<33.6 psu) was still observed at Stations G, P, and I, which suggests that there was a significant gap between each observation time in the survey at different locations because there should not be such a large difference in the SSS at adjacent stations. The difference between the survey and satellite water mass data was very significant in winter. The results in the northern PHC (Stations A–F) showed low SST and low SSS values from the satellite, which is characteristic of the MCCW and NTMW, while the survey only observed such water masses at point B. In the case of strong northeasterly winds, the flow characteristics in the northern PHC were close to those of the MCCW and NTMW, which were carried southward by the NTCC. In addition, it was difficult to conduct the survey under rough sea conditions. Therefore, the results of the water mass were close to the KBW at most survey stations in winter.

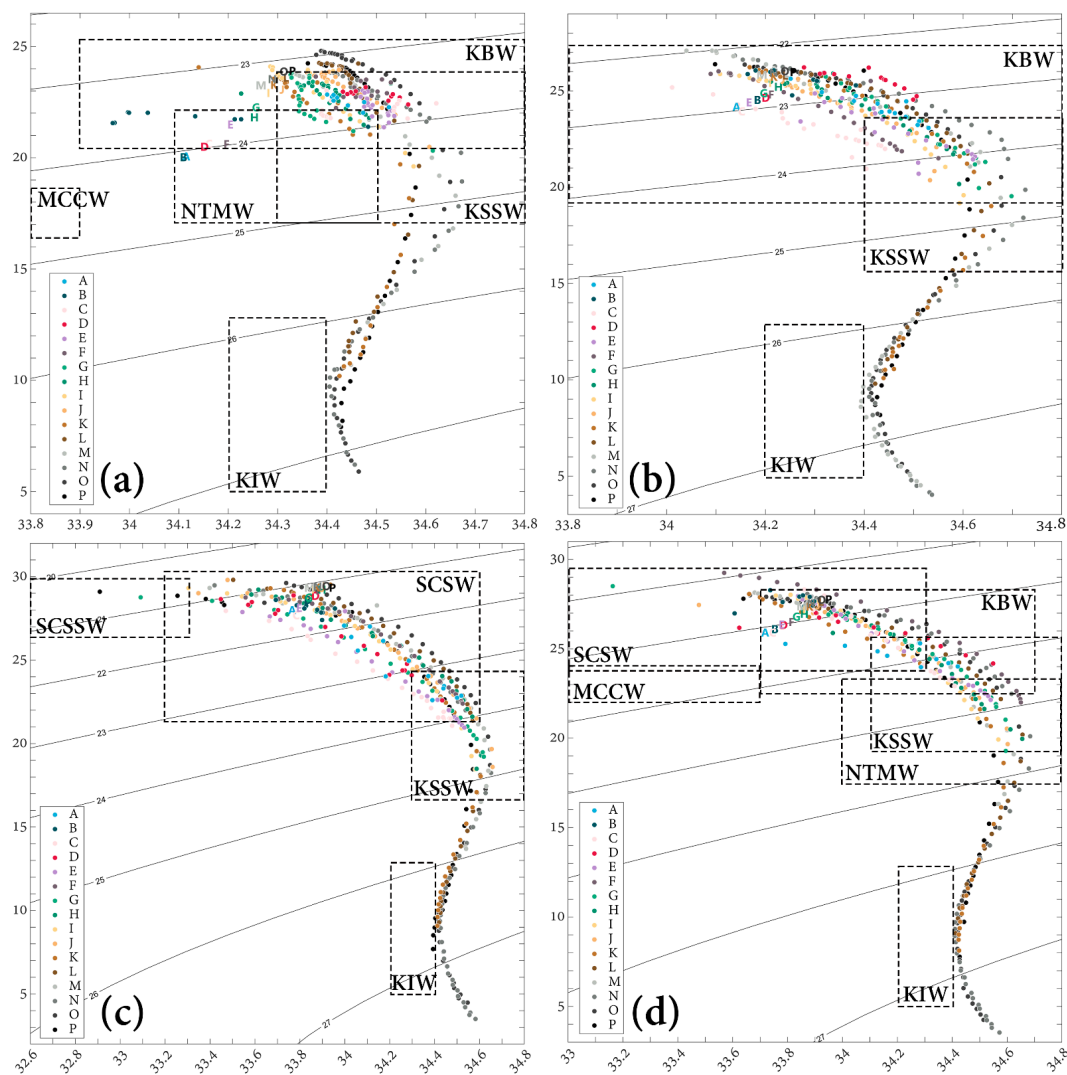


Figure 14. The water mass types of the PHC in each season observed from the historical survey. The horizontal and vertical coordinates represent salinity (psu) and temperature (°C), respectively. (a) Winter, (b) spring, (c) summer, and (d) fall. Each color dot represents the results of each site location. Capital letters represent the long-term average results of satellite observations of SST and SSS (Figures 11 and 13).

Table 1. Temperature and salinity of the main water masses in each season adjacent to the PHC. Full names of each water mass: KBW (Kuroshio Branch Water), KIW (Kuroshio Intermediate Water), KSSW (Kuroshio Sub-Surface Water), MCCW (Mixed China Coastal Water), NTMW (Northern Taiwan Mixed Water), SCSW (South China Sea Water), and SCSSW (South China Sea Surface Water).

	Temperature (°C)				Salinity (psu)			
	Winter	Spring	Summer	Fall	Winter	Spring	Summer	Fall
KBW	20.4–25.4	19.1–27.4	–	22.5–28.2	33.9–34.8	33.8–34.8	–	33.7–34.7
KIW		5.0–12.8				34.2–34.4		
KSSW	17.1–23.7	15.6–23.7	16.7–24.2	19.2–25.7	34.3–34.8	34.4–34.8	34.3–34.8	34.1–34.8
MCCW	16.4–18.6	–	–	22.0–24.0	32.7–33.9	–	–	31.8–33.7
NTMW	17.1–23.1	–	–	17.4–23.4	34.1–34.7	–	–	34.0–34.8
SCSW	–	–	21.2–30.2	23.7–29.5	–	–	33.2–34.6	32.6–34.3
SCSSW	–	–	26.3–29.9	27.8–29.2	–	–	32.5–33.3	31.4–32.6

5. Conclusions

It is necessary to consider various observation data to analyze the ocean characteristics of coastal areas. Satellite, cruise survey, drifter, and HF radar data were used to observe changes in ocean surface currents near the PHC both hourly and through climatological seasons in this study. The HF radar observation results helped to clarify the variations of the flow field, presenting the characteristics of the current direction and speed affected by the significant seasonal wind field and semidiurnal tidal currents in the PHC which cannot be found in satellite geostrophic flow fields. The HF radar flow field data with a 10 km spatial resolution enabled researchers to analyze the nearshore flow, which will help to analyze the dynamics of the coastal ocean environment by combining high-resolution SST and Chl-a satellite data in the future. Using the drifter data based on the Lagrangian observation method, this study not only provided evidence that the ocean current southward passes through the PHC in fall and winter but also observed the near-inertial oscillation and trajectories trapped by a mesoscale eddy in southwestern Taiwan, which can be combined with HF radar data to analyze the ocean physical process in the future. The importance and necessity of long-term HF radar observations were confirmed through a comparison of various data. Notably, the satellite geostrophic data in TS may not represent the real ocean current conditions. Additionally, the survey observation data should be carefully used because this dataset, collected at a specific time, cannot represent the characteristics of the entire season.

This study suggests that the direction and intensity of the ocean wind significantly change the ocean flow field in the PHC. In winter and fall, the strong northerly winds cause the southward NTCC along the coast of Taiwan to enter the PHC, carrying water masses of the NTMW and MCCW. The northward flow in the PHC is the KBW or SCSW under a weak northerly wind and even southerly wind. In spring and summer, change in the wind direction does not result in the presence of the main northward KBW or SCSW. Instead, it slightly changes the flow path and speed after flowing through the PHC. The hourly tidal current speed in the PHC area can reach more than 1 m/s, whereas the average daily flow speed is 0.17 m/s. The HF radar results not only properly solve the problem of the characteristic variation in the PHC surface current but also are consistent with the satellite observations of long-term average SST, SSS, and Chl-a. This research will help oceanographers with different areas of expertise to better understand the TS area, enabling them to conduct more in-depth research on changes at smaller scales and in shorter timeframes in the future.

Funding: This work was supported by the Ministry of Science and Technology of Taiwan through grant 110-2611-M-008-007.

Data Availability Statement: The satellite ocean currents data are distributed through the Copernicus Marine and Environment Monitoring Service (SEALEVEL_GLO_PHY_L4_MY_008_047, <https://doi.org/10.48670/moi-00148> (accessed on 9 February 2022)). The coastal radar data are available through TOROS (<https://www.tori.narl.org.tw/ETORI/eDefault.aspx> (accessed on 9 February 2022)). The drifter data were downloaded from National Oceanic and Atmospheric Administration Atlantic Oceanographic and Meteorological Laboratory Physical Oceanography Division (<https://www.aoml.noaa.gov/phod/gdp/index.php> (accessed on 9 February 2022)). The historical ADCP data and hydrological observations data are available through the ODB of the Ministry of Science and Technology, Taiwan (<http://www.odb.ntu.edu.tw/en/> (accessed on 9 February 2022)). The sea surface temperature and chlorophyll-a data of Himawari-8 satellite were supplied by the P-Tree System, Japan Aerospace Exploration Agency (JAXA) (<http://www.eorc.jaxa.jp/ptree/> (accessed on 9 February 2022)). The sea surface salinity data are distributed through the Copernicus Marine and Environment Monitoring Service (MULTIOBS_GLO_PHY_S_SURFACE_MYNRT_015_013, <https://doi.org/10.48670/moi-00051> (accessed on 9 February 2022)). The ocean wind data are distributed through the Copernicus Marine and Environment Monitoring Service (WIND_GLO_PHY_CLIMATE_L4_REP_012_003, <https://doi.org/10.48670/moi-00181> (accessed on 9 February 2022)). C-2015 ASCAT data are produced by remote sensing systems and sponsored by the NASA Ocean Vector Winds Science Team. Data are available at www.remss.com (accessed on 9 February 2022).

Acknowledgments: The author appreciates all the data used provided from each open database. The author thanks anonymous reviewers and academic editors for their comments.

Conflicts of Interest: The author declares no conflict of interest.

Appendix A

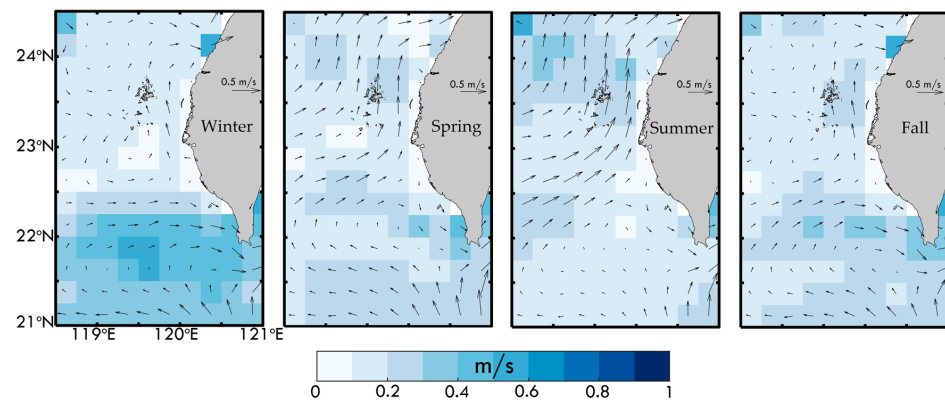


Figure A1. Climatological seasonal satellite-derived geostrophic ocean currents (vector) averaged and speed variance (shading) over time from 1993 to 2020.

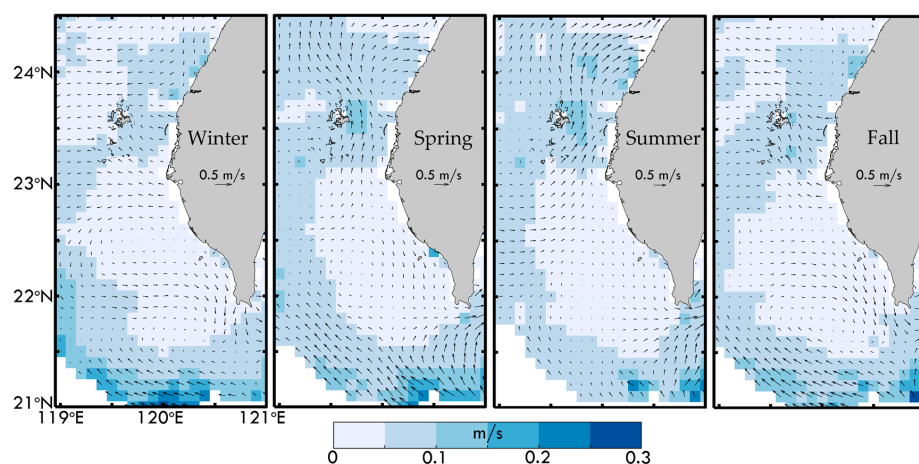


Figure A2. Climatological seasonal flow field (vector) averaged and speed variance (shading) from hourly HF radar data from December 2014 to December 2020.

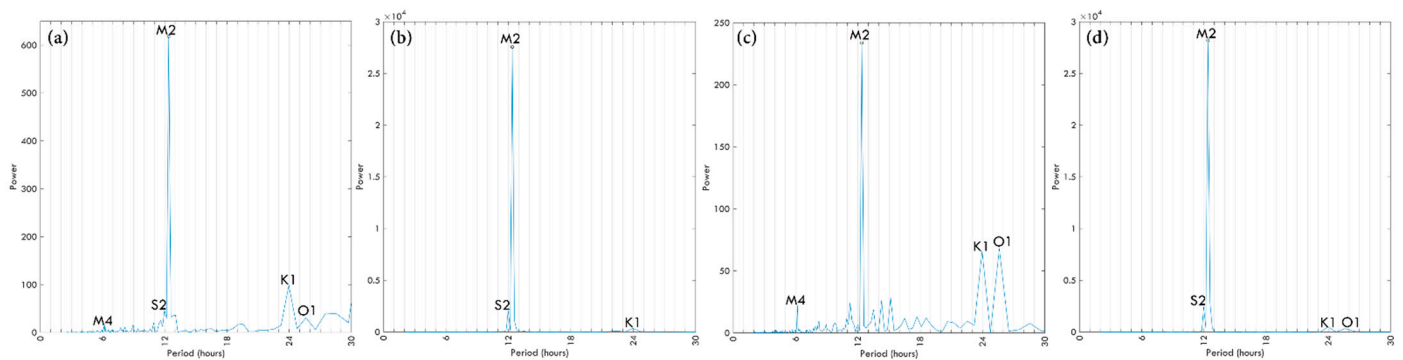


Figure A3. Power spectrum based on the fast Fourier transform analysis of (a) Figure 9a, (b) Figure 9b, (c) Figure 9c, and (d) Figure 9d. The dominant tidal constituents: M2 (principal lunar semidiurnal), S2 (principal solar semidiurnal), K1 (luni-solar declinational diurnal), O1 (principal lunar declinational diurnal), and M4 (shallow water overtides of principal lunar).

References

- Huang, Z.Y.; Yu, H.S. Morphology and geologic implications of Penghu Channel off southwest Taiwan. *Terr. Atmos. Ocean. Sci.* **2003**, *14*, 469–486. [[CrossRef](#)]
- Hsiung, K.H.; Yu, H.S.; Su, M. Sedimentation in remnant ocean basin off SW Taiwan with implication for closing northeastern South China Sea. *J. Geol. Soc.* **2015**, *172*, 641–647. [[CrossRef](#)]
- Chen, W.B.; Liu, W.C. Assessing the influence of sea level rise on tidal power output and tidal energy dissipation near a channel. *Renew. Energy* **2017**, *101*, 603–616. [[CrossRef](#)]
- Hu, Z.; Qi, Y.; He, X.; Wang, Y.H.; Wang, D.P.; Cheng, X.; Liu, X.; Wang, T. Characterizing surface circulation in the Taiwan Strait during NE monsoon from Geostationary Ocean Color Imager. *Remote Sens. Environ.* **2019**, *221*, 687–694. [[CrossRef](#)]
- Shao, H.J.; Tseng, R.S.; Lien, R.C.; Chang, Y.C.; Chen, J.M. Turbulent mixing on sloping bottom of an energetic tidal channel. *Cont. Shelf Res.* **2018**, *166*, 44–53. [[CrossRef](#)]
- Hsu, P.C.; Centurioni, L.; Shao, H.J.; Zheng, Q.; Lu, C.Y.; Hsu, T.W.; Tseng, R.S. Surface Current Variations and Oceanic Fronts in the Southern East China Sea: Drifter Experiments, Coastal Radar Applications, and Satellite Observations. *J. Geophys. Res. Ocean.* **2021**, *126*, e2021JC017373. [[CrossRef](#)]
- Fang, W.P.; Wu, D.R.; Zheng, Z.W.; Gopalakrishnan, G.; Ho, C.R.; Zheng, Q.; Huang, C.F.; Ho, H.; Weng, M.C. Impacts of the Kuroshio intrusion through the Luzon Strait on the local precipitation anomaly. *Remote Sens.* **2021**, *13*, 1113. [[CrossRef](#)]
- Jan, S.; Wang, J.; Chern, C.S.; Chao, S.Y. Seasonal variation of the circulation in the Taiwan Strait. *J. Mar. Syst.* **2002**, *35*, 249–268. [[CrossRef](#)]
- Lan, K.W.; Kawamura, H.; Lee, M.A.; Chang, Y.; Chan, J.W.; Liao, C.H. Summertime sea surface temperature fronts associated with upwelling around the Taiwan Bank. *Cont. Shelf Res.* **2009**, *29*, 903–910. [[CrossRef](#)]
- Bai, Y.; Huang, T.H.; He, X.; Wang, S.L.; Hsin, Y.C.; Wu, C.R.; Zhai, W.; Lui, H.K.; Chen, C.T.A. Intrusion of the Pearl River plume into the main channel of the Taiwan Strait in summer. *J. Sea Res.* **2015**, *95*, 1–15. [[CrossRef](#)]
- Kuo, Y.C.; Lee, M.A.; Chuang, C.C.; Ma, Y.P. Long-term AVHRR SST change analysis in the Taiwan Strait using the rotated EOF method. *Terr. Atmos. Ocean. Sci.* **2017**, *28*, 1–10. [[CrossRef](#)]
- Lee, M.A.; Huang, W.P.; Shen, Y.L.; Weng, J.S.; Semedi, B.; Wang, Y.C.; Chan, J.W. Long-Term Observations of Interannual and Decadal Variation of Sea Surface Temperature in the Taiwan Strait. *J. Mar. Sci. Technol.* **2021**, *29*, 7. [[CrossRef](#)]
- Huang, T.H.; Chen, C.T.A.; Zhang, W.Z.; Zhuang, X.F. Varying intensity of Kuroshio intrusion into Southeast Taiwan Strait during ENSO events. *Cont. Shelf Res.* **2015**, *103*, 79–87. [[CrossRef](#)]
- Huang, T.H.; Lun, Z.; Wu, C.R.; Chen, C.T.A. Interannual carbon and nutrient fluxes in southeastern Taiwan Strait. *Sustainability* **2018**, *10*, 372. [[CrossRef](#)]
- Huang, T.H.; Chen, C.T.A.; Bai, Y.; He, X. Elevated primary productivity triggered by mixing in the quasi-cul-de-sac Taiwan Strait during the NE monsoon. *Sci. Rep.* **2020**, *10*, 7846. [[CrossRef](#)] [[PubMed](#)]
- Tseng, H.C.; You, W.L.; Huang, W.; Chung, C.C.; Tsai, A.Y.; Chen, T.Y.; Lan, K.W.; Gong, G.C. Seasonal variations of marine environment and primary production in the Taiwan Strait. *Front. Mar. Sci.* **2020**, *38*. [[CrossRef](#)]
- Wu, Y.L.; Lee, M.A.; Chen, L.C.; Chan, J.W.; Lan, K.W. Evaluating a suitable aquaculture site selection model for Cobia (*Rachycentron canadum*) during extreme events in the inner bay of the Penghu Islands, Taiwan. *Remote Sens.* **2020**, *12*, 2689. [[CrossRef](#)]
- Ko, D.S.; Chao, S.Y.; Wu, C.C.; Lin, I.I.; Sen, J. Impacts of tides and Typhoon Fanapi (2010) on seas around Taiwan. *Terr. Atmos. Ocean. Sci.* **2016**, *27*, 2. [[CrossRef](#)]
- Shen, J.; Li, L.; Zhu, D.; Liao, E.; Guo, X. Observation of abnormal coastal cold-water outbreak in the Taiwan Strait and the cold event at Penghu waters in the beginning of 2008. *J. Mar. Syst.* **2020**, *204*, 103293. [[CrossRef](#)]

20. Jan, S.; Chao, S.Y. Seasonal variation of volume transport in the major inflow region of the Taiwan Strait: The Penghu Channel. *Deep. Sea Res. Part II Top. Stud. Oceanogr.* **2003**, *50*, 1117–1126. [[CrossRef](#)]
21. Wu, C.R.; Hsin, Y.C. Volume transport through the Taiwan Strait: A numerical study. *Terr. Atmos. Ocean. Sci.* **2005**, *16*, 377. [[CrossRef](#)]
22. Qiu, Y.; Li, L.; Chen, C.T.A.; Guo, X.; Jing, C. Currents in the Taiwan Strait as observed by surface drifters. *J. Oceanogr.* **2011**, *67*, 395–404. [[CrossRef](#)]
23. Wang, L.; Pawlowicz, R.; Wu, X.; Yue, X. Wintertime Variability of Currents in the Southwestern Taiwan Strait. *J. Geophys. Res. Ocean.* **2021**, *126*, e2020JC016586. [[CrossRef](#)]
24. Shen, J.; Zhang, J.; Qiu, Y.; Li, L.; Zhang, S.; Pan, A.; Huang, J.; Guo, X.; Jing, C. Winter counter-wind current in western Taiwan Strait: Characteristics and mechanisms. *Cont. Shelf Res.* **2019**, *172*, 1–11. [[CrossRef](#)]
25. Tseng, Y.H.; Lu, C.Y.; Zheng, Q.; Ho, C.R. Characteristic Analysis of Sea Surface Currents around Taiwan Island from CODAR Observations. *Remote Sens.* **2021**, *13*, 3025. [[CrossRef](#)]
26. Roarty, H.; Cook, T.; Hazard, L.; George, D.; Harlan, J.; Cosoli, S.; Wyatt, L.; Alvarez Fanjul, E.; Terrill, E.; Otero, M.; et al. The global high frequency radar network. *Front. Mar. Sci.* **2019**, *6*, 164. [[CrossRef](#)]
27. Shen, Y.T.; Lai, J.W.; Leu, L.G.; Lu, Y.C.; Chen, J.M.; Shao, H.J.; Tseng, R.S. Applications of ocean currents data from high-frequency radars and current profilers to search and rescue missions around Taiwan. *J. Oper. Oceanogr.* **2019**, *12*, S126–S136. [[CrossRef](#)]
28. Elipot, S.; Lumpkin, R.; Perez, R.C.; Lilly, J.M.; Early, J.J.; Sykulski, A.M. A global surface drifter data set at hourly resolution. *J. Geophys. Res. Ocean.* **2016**, *121*, 2937–2966. [[CrossRef](#)]
29. Kurihara, Y.; Murakami, H.; Kachi, M. Sea surface temperature from the new Japanese geostationary meteorological Himawari-8 satellite. *Geophys. Res. Lett.* **2016**, *43*, 1234–1240. [[CrossRef](#)]
30. Kurihara, Y.; Murakami, H.; Ogata, K.; Kachi, M. A quasi-physical sea surface temperature method for the split-window data from the Second-generation Global Imager (SGLI) onboard the Global Change Observation Mission-Climate (GCOM-C) satellite. *Remote Sens. Environ.* **2021**, *257*, 112347. [[CrossRef](#)]
31. Murakami, H. Ocean color estimation by Himawari-8/AHI. In *Remote Sensing of the Oceans and Inland Waters: Techniques, Applications, and Challenges*; SPIE Asia-Pacific Remote Sensing: New Delhi, India, 2016; Volume 9878, pp. 177–186.
32. Droghei, R.; Buongiorno Nardelli, B.; Santoleri, R. A new global sea surface salinity and density dataset from multivariate observations (1993–2016). *Front. Mar. Sci.* **2018**, *5*, 84. [[CrossRef](#)]
33. Jan, S.; Sheu, D.D.; Kuo, H.M. Water mass and throughflow transport variability in the Taiwan Strait. *J. Geophys. Res. Ocean.* **2006**, *111*. [[CrossRef](#)]
34. Hsu, P.C.; Lee, H.J.; Lu, C.Y. Impacts of the Kuroshio and Tidal Currents on the Hydrological Characteristics of Yilan Bay, Northeastern Taiwan. *Remote Sens.* **2021**, *13*, 4340. [[CrossRef](#)]
35. Chen, C.T.A. Chemical and physical fronts in the Bohai, Yellow and East China seas. *J. Mar. Syst.* **2009**, *78*, 394–410. [[CrossRef](#)]
36. Qu, B.; Song, J.; Yuan, H.; Li, X.; Li, N. Carbon chemistry in the mainstream of Kuroshio current in eastern Taiwan and its transport of carbon into the east China sea shelf. *Sustainability* **2018**, *10*, 791. [[CrossRef](#)]
37. Hsu, P.C.; Ho, C.R. Typhoon-induced ocean subsurface variations from glider data in the Kuroshio region adjacent to Taiwan. *J. Oceanogr.* **2019**, *75*, 1–21. [[CrossRef](#)]